International Journal of Heat and Fluid Flow 31 (2010) 295–306

Contents lists available at ScienceDirect

International Journal of Heat and Fluid Flow

journal homepage: www.elsevier.com/locate/ijhff

Direct numerical simulation of flow separation behind a rounded leading edge: Study of curvature effects

Eric Lamballais [a,*], Jorge Silvestrini [b], Sylvain Laizet [a,c]

[a] Institute PPRIME, Department of Fluid Flow, Heat Transfer and Combustion, Université de Poitiers, ENSMA, CNRS, Téléport 2 – Bd. Marie et Pierre Curie B.P. 30179, 86962 Futuroscope Chasseneuil Cedex, France

[b] Faculdade de Engenharia, Pontifícia Universidade Católica do Rio Grande do Sul, Av. Ipiranga 6681, 90619-900 Porto Alegre – RS, Brazil

[c] Department of Aeronautics, Institute for Mathematical Sciences, Imperial College London, South Kensington Campus, London SW7 2AZ, UK

ARTICLE INFO

Article history:
Received 7 September 2009
Received in revised form 4 December 2009
Accepted 9 December 2009
Available online 22 January 2010

Keywords:
Separation bubble
Direct numerical simulation of turbulence
Immersed boundary method
Inflow condition receptivity
Self-excited mechanisms

ABSTRACT

The separation bubble formed over a 2D half-body is studied by direct numerical simulation. The aim of this work is to consider the physical influence of the shape of the body that can be viewed as a thick half-plate with a front edge more or less rounded. The present generic body geometry is defined with a unique parameter $\eta = R/H$ corresponding to the ratio of the curvature radius R of the front edge over the body height H. In this paper, 18 calculations are presented depending on: (i) the value of η with $\eta = 0.125,\ 0.25,\ 0.5,\ 1$; (ii) the 2D/3D nature of the computation; (iii) the inflow perturbations used to mimic residual turbulence in the free stream velocity U_∞. Only one Reynolds number $Re = U_\infty H/\nu$ is used for every simulation, allowing us to focus on the curvature effects over the separation bubble dynamics. The value of the Reynolds number ($Re = 2000$) combined with the resolution demand of the front edge (close to a sharp corner for the highest curvature case) requires to simulate the flow using up to 876 million mesh nodes. The curvature effects are found to deeply influence the separation bubble dynamics, with a significant expansion of the separated region size predicted by 3D computations. This expansion is driven by the separation angle rise combined with the reinforcement of turbulence levels as the curvature is increased. These trends are associated with a change of bubble sensitivity with respect to upstream/downstream perturbations that can be interpreted in terms of convective/absolute stability.

© 2010 Elsevier Inc. All rights reserved.

1. Introduction

In many practical situations, flow separation is triggered by a sharp edge. In the context of bluff body, edges can be advantageously smoothed to improve the aerodynamic characteristics of the body while better controlling the production of noise or vibrations. Despite the practical knowledge of these types of influence (especially in the car industry), there is no clear understanding of the physical mechanisms involved in the change of the resulting flow separation depending on the shape of the edge. In this study, our goal is to focus on these effects by considering a generic configuration where the flow separates over a rounded edge. The change of dynamics will be analyzed through its influence on: (i) the mean flow (separation bubble features); (ii) the production of turbulent kinetic energy; (iii) the receptivity with respect to inflow perturbations.

In a previous study (Lamballais et al., 2008), we already have considered by direct numerical simulation (DNS) the curvature effects through comparisons between 2D and 3D flow separations behind two different front edges more or less rounded. Because interesting behaviours have been observed for a purely 2D body, our purpose in this work is to focus on this type of geometry by considering a wider range of rounded edges. Additionally, in order to reduce the influence of viscous effects on the dynamics, a higher Reynolds number is considered while maintaining the DNS strategy. This improvement of our results in terms of realism has required to increase drastically the computational effort with the help of the new generation of supercomputers.

This paper is organised as follows. In Section 2, the physical and numerical configurations are introduced. In the following three sections, the results are presented through analysis of instantaneous visualizations (Section 3), the mean flow (section 4) and the turbulent kinetic energy (Section 5). Then, the question of the receptivity of the flow with respect to upstream conditions is addressed in terms of statistical (Section 6) and deterministic (Section 7) sensitivity that is associated with the backflow inside the bubble (Section 8). Finally, the main conclusions of this study are summarized in Section 9.

* Corresponding author. Tel.: +33 5 49 49 69 68.
E-mail addresses: lamballais@univ-poitiers.fr (E. Lamballais), jorgehs@pucrs.br (J. Silvestrini), s.laizet@imperial.ac.uk (S. Laizet).

0142-727X/$ - see front matter © 2010 Elsevier Inc. All rights reserved.
doi:10.1016/j.ijheatfluidflow.2009.12.007

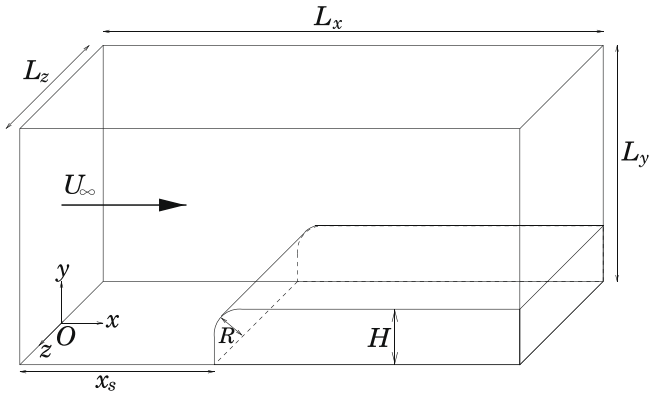

Fig. 1. Schematic view of the flow configuration.

2. Flow configuration and numerical method

2.1. Flow configuration

In this paper, we consider the flow over a semi-infinite 2D body presenting a single curved leading edge. The flow configuration is presented in Fig. 1. Only a half model is considered through the imposition of mirror conditions (i.e. free-slip) at $y = 0$. This assumption allows the reduction of the computational storage by a factor two while fixing by construction the location of the stagnation point at $(x,\ y) = (x_s,\ 0)$ with $x_s = 8H$. The present body geometry is fully determined by its height H and its constant edge radius R, with a unique nondimensional parameter $\eta = R/H$ with $0 \leqslant \eta \leqslant 1$. The value $\eta = 0$ refers to an infinitely sharp edge (square corner) while $\eta = 1$ corresponds to a perfectly rounded leading edge over its full height (quarter round). Using the constant mean velocity U_∞ at the inflow section as reference velocity, the Reynolds number can be defined as $Re = U_\infty H/\nu$. Basically, the flow configuration in an infinite domain free from any perturbations is fully determined by the parameter couple η and Re. In this paper, four different curvatures are examined with $\eta = 0.125,\ 0.25,\ 0.5,\ 1$. To better identify the 3D effects, especially inside the separation bubble, these four flow geometries are compared using 3D and 2D DNS with and without inflow perturbations. Two additional 3D DNS (for $\eta = 0.25,\ 1$) based on a strong inlet excitation are also presented.

2.2. Numerical method

To simulate the flow, the DNS code "Incompact3d" is used in a recent version adapted to parallel supercomputers (Laizet et al., 2010). This code is based on compact sixth-order finite difference schemes for the spatial differentiation and a second order Adams–Bashforth scheme for the time integration (Laizet and Lamballais, 2009). The incompressible Navier–Stokes equations are directly solved in a computational domain $L_x \times L_y \times L_z$ on a Cartesian mesh (regular in $x,\ z$ and stretched in y). The presence of the body is modelled with an immersed boundary method (IBM) adapted to the use of high-order schemes (Parnaudeau et al., 2008).

For the present study, an improvement of the method is carried out with the help of an extra-dissipation introduced artificially via the viscous term. This opportunity is offered by the use of compact schemes to compute second derivatives. This family of finite difference scheme can be easily adjusted to be over-dissipative on a narrow range of scales in the neighbourhood of the cutoff wave number associated with the mesh. For a linear convection/diffusion equation, it can be shown that this extra-dissipation is more concentrated at the highest wave numbers (allowed by the mesh) than the one introduced by high-order upwind schemes, even in a low-dissipation formulation like in Adams and Shariff (1996). This

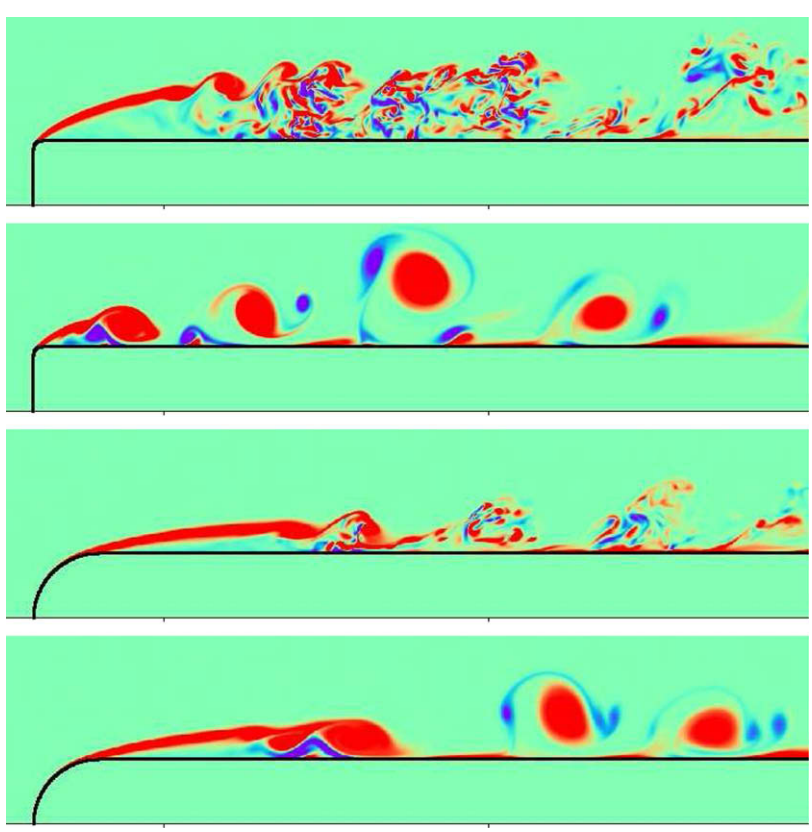

Fig. 2. Maps of spanwise vorticity ω_z. From top to bottom: $\eta = 0.125$ (3D), $\eta = 0.125$ (2D), $\eta = 1$ (3D), $\eta = 1$ (2D). DNS with inflow perturbations $u'_{\text{inflow}} = 0.1\%U_\infty$.

numerical treatment is very easy to implement without any significant computational extra-cost contrary to the use of an upwind formulation. It is also more effective and cheaper for the control of aliasing errors (non-negligible when high-order schemes are used) by comparison with a compact filtering of the non-linear terms for the present calculations. Moreover, the small wiggles created by the use of an IBM are also better reduced by the extra-dissipation compared with a filtering procedure. Here, only a local and explicit filtering of the non-linear terms is performed through a small patch located in front of the half-body. The use of this patch has been found to slightly improve the regularity of the solution in the near-body region without any detectable effects on the dynamics of the flow. Finally, note that the numerical viscosity introduced by the present discretization (for details about the coefficients of the finite difference scheme used in this study, see Laizet and Lamballais, 2009) is only concentrated at the highest wave numbers so that it cannot replace a subgrid-scale model in the context of large eddy simulation (LES). Therefore, present DNS should not be viewed as implicit LES but instead as DNS performed at marginal resolution (with respect to the Reynolds number) with a slight regularization procedure to control wiggles introduced by aliasing errors and the IBM forcing.

2.3. Physical and numerical parameters

Two types of mesh are used in the same computational domain $L_x \times L_y \times L_z = 20.25H \times 16H \times 6H$. For the moderate curvature cases $\eta = 0.25,\ 0.5,\ 1$, the use of $n_x \times n_y \times n_z = 1621 \times 451 \times 300$ mesh nodes allows us to reach $Re = 2000$ with a satisfactory numerical accuracy. Note that this spatial resolution ensures to describe the rounded edge geometry using at least 20 mesh nodes by curvature radius. To preserve this criterion, the case $\eta = 0.125$ has required to use a grid of $n_x \times n_y \times n_z = 3241 \times 901 \times 300$ mesh nodes while considering the same Reynolds number. For the 2D DNS $(n_z = 1,\ L_z = \infty)$, exactly the same resolutions have been used. The boundary conditions imposed are inflow/outflow in x, free-slip in y and for 3D calculations, periodicity in z.

The inflow velocity $(U_\infty,\ 0,\ 0)$ can be perturbed through the superimposition of velocity fluctuations $(u',\ v',\ w')$ where each component corresponds to a low amplitude noise (without cross-correlation) with the same root mean square $u'_{\text{inflow}} = 0.1\%,\ 1\%U_\infty$. This noise is computed to excite randomly and equally (in mean) all the length scales up to a cutoff wavelength of $H/6$ with a perfect time periodicity of $T = 40H/U_\infty$. Note that we have checked in a preliminary spectral analysis of the velocity fluctuations further downstream (inside and behind the separation bubble) that this time periodicity does not introduce any artificial dominant frequency (for instance $f = 1/T$), the flow being found to develop its intrinsic instabilities with similar frequencies with or without inflow perturbations. Statistics are collected on a duration multiple of this particular period (after a transient stage to obtain a well established flow) with an additional average in the homogeneous z-direction for 3D calculations. The marginal statistical convergence reached by 3D DNS using only two periods $(2T = 80H/U_\infty)$ has been considered enough as far as the following analyses are concerned. Naturally, a quantitative study of low frequency phenomena would require to consider a clearly larger integration time to provide accurate statistics. For present 2D DNS, due to the lack of average in z-direction, we have used at least forty periods $(40T = 1600H/U_\infty)$ to reach an acceptable statistical convergence.

As already mentioned, the present study is based on 18 calculations where four different front-edge curvatures are considered by 2D and 3D DNS with and without inflow perturbations. All the data issued from these calculations have been exploited but in the rest of this paper, only a selection of results is presented to highlight the influence of η on the separation dynamics.

3. Instantaneous visualizations

First, some comments should be made about results from 2D DNS. It is well known that the 2D assumption can lead to an unrealistic flow especially for the present separated flow that is highly unstable with respect to 3D perturbations. In consequence, present 2D DNS should be viewed as a reduced model where 3D motions are artificially prevented without expecting any relevancy with respect to the corresponding flow in real life. This point is illustrated in Fig. 2 where spanwise vorticity maps are compared from 2D and 3D DNS for the two extreme curvatures considered here, namely $\eta = 0.125,\ 1$. The resulting 2D dynamics is shown to differ drastically from the 3D one, with a quasi-periodic shedding of very large scale vortices from the bubble separation. For these structures, clockwise vortices (of same vorticity as the shear layer at the start of the separation) dominate their counterclockwise counterparts formed in the near-wall region inside the separation. For the 3D

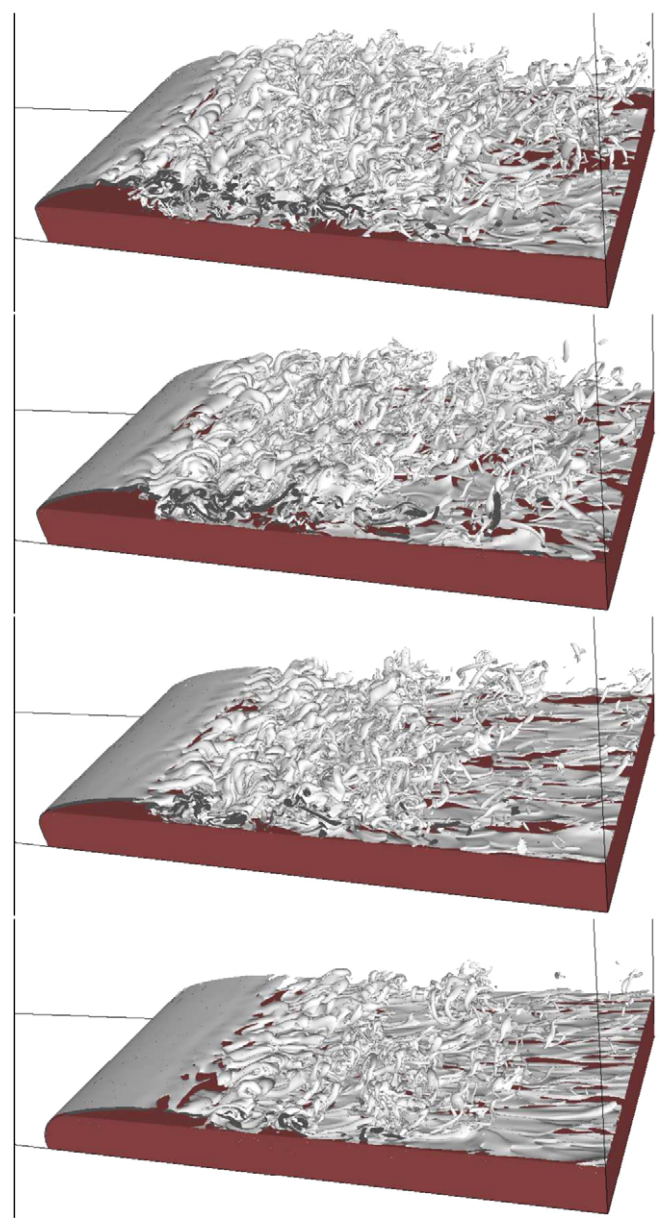

Fig. 3. Perpective views of vorticity modulus isosurface $\omega = 8U_\infty/H$ for $\eta = 0.125,\ 0.25,\ 0.5,\ 1$ (from top to bottom). Results from 3D DNS with inflow perturbations $u'_{\text{inflow}} = 0.1\%U_\infty$.

results, a comparable formation of nearly-2D Kelvin–Helmholtz vortices can be recovered, but further downstream, the occurrence of a turbulence breakdown destroys the 2D coherence of the large scale structures as they travel through and behind the separation (see also Fig. 3).

A more complete view of the 3D dynamics can be obtained by volume visualizations of a characteristic vorticity isosurface as presented in Fig. 3 for the four curvatures considered. This type of view reveals clearly the highly 3D nature of the flow structures that develop in the separated region of the flow. Qualitatively, comparisons between the different body geometries show that the separation is deeply modified by the shape of the front edge with a more marked turbulent behaviour when the curvature is high. The breakdown to turbulence occurs clearly earlier as the

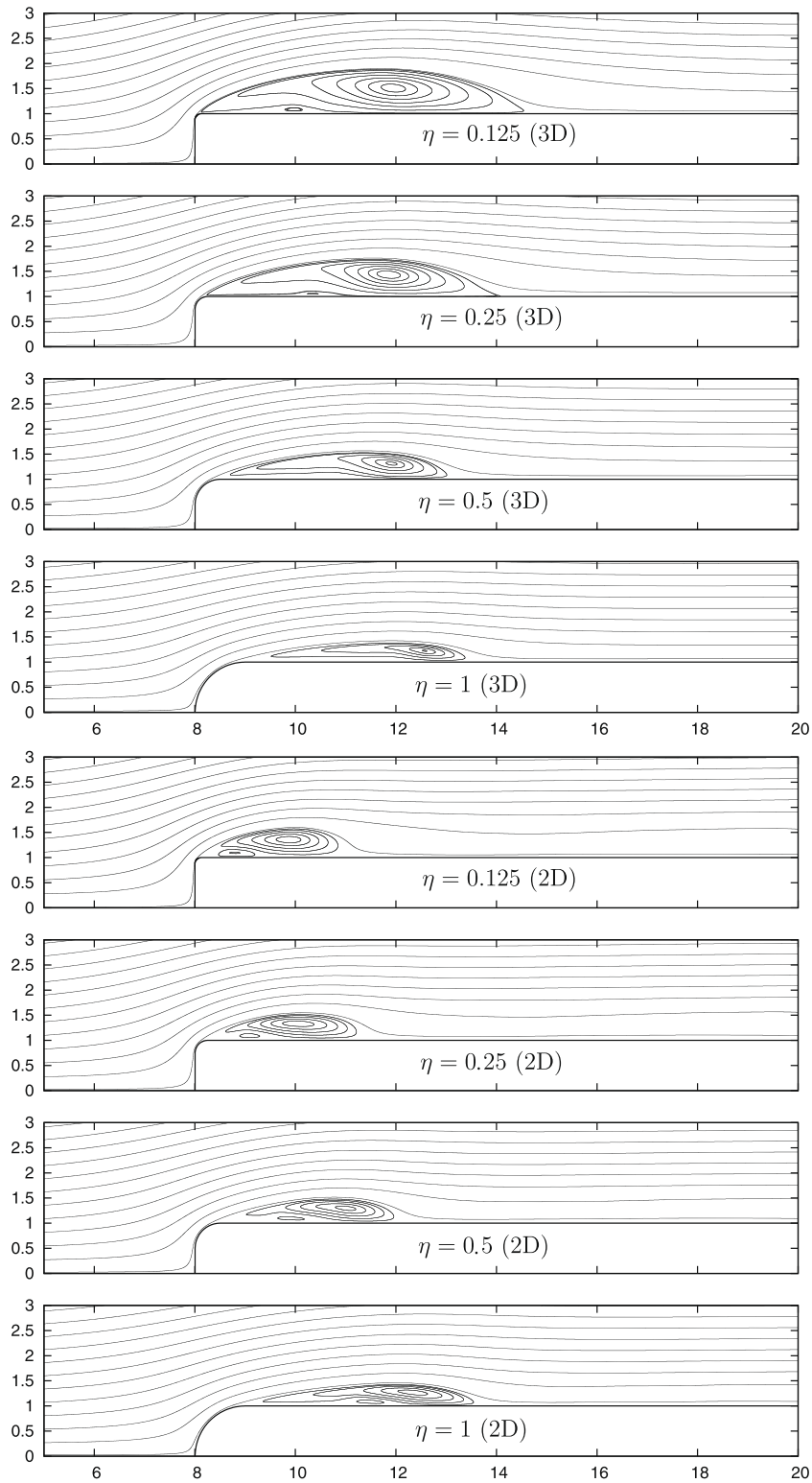

Fig. 4. Mean streamlines for $\eta = 0.125,\ 0.25,\ 0.5,\ 1$. Results from 3D and 2D DNS with inflow perturbations $u'_{\text{inflow}} = 0.1\% U_\infty$.

curvature is increased (i.e. $\eta \downarrow$) through the appearance of small scale longitudinal vortices that fill the separated region. The resulting levels of vorticity are increased accordingly with a simultaneous scale reduction of the vortical structures, giving the impression of an increase of the Reynolds number for a larger leading-edge curvature. Schematically, the observation of present visualizations suggests that when the front edge is sharper, the turbulence activity inside the separation bubble is reinforced through physical mechanisms involving the direct excitation of the separated shear layer. This point will be addressed in the following.

4. Bubble separation features

The examination of the mean flow allows the straightforward differentiation of the separation bubble obtained in each case. Here, we focus on the bubble size measured through its longitudinal and vertical expansion given by its reattachment length l_r and height h_r respectively. Note that l_r is estimated as $x_r - x_0$ where x_r is the streamwise location where the mean flow reattaches (detected here via the sign change of the longitudinal mean velocity at the first mesh node above the wall) while x_0 designates the end location of the body curvature ($x_0 = x_s + R$) where the separation is nearly observed for all the cases considered. The resulting mean flow patterns are presented in Fig. 4 where some selected streamlines are plotted to highlight the separation bubble shape. Only cases with inflow perturbations $u'_{\text{inflow}} = 0.1\% U_\infty$ are discussed in this section, the bubble separation structure being qualitatively similar without inlet excitation (for quantitative information, see Table 1). As it can be expected, the changes between 2D and 3D dynamics lead to different mean flows as revealed by important modifications of the separation bubble shape.

In terms of curvature effects, the reduction of η is found to shorten significantly l_r in 2D (up to -29%) while the opposite trend is observed in 3D (up to +45%), as shown by Table 1 and illustrated in Fig. 5. The 2D/3D differences of the bubble shape are less pronounced in its upstream part with virtually no modification of the separation angle θ (defined here as the direction of the mean flow at $x = x_0$ with respect to the horizontal direction). This suggests that the separation start remains purely 2D with a minor influence of downstream perturbations. The major influence of the separation angle is due to the body geometry where θ goes from 15° at the lowest curvature ($\eta = 1$) to 40° at the highest one ($\eta = 0.125$) as shown in Fig. 6. This change of the separation orientation leads to an increase of h_r when the curvature is increased (see Table 1 and Fig. 7).

For a steady flow, it can be expected that a θ increase leads also to a l_r increase. However, for an unsteady separation, high turbulence levels are known to reduce the recirculation zone. Because the reduction of the curvature radius is found to increase the turbulence levels, two antagonist effects are present. The combination of these two opposite influences leads to a reduction of l_r in 2D through the very high velocity fluctuations induced by the large scale vortices that control directly the reattachment. For the more realistic 3D dynamics, the turbulence breakdown leads to weaker velocity fluctuations (by comparison to the 2D case) so that the behaviour of l_r corresponds to what it can be expected for the steady case, namely a l_r increase when θ is high (i.e. for high curvature).

Present l_r value for $\eta = 1$ in the 3D case is in good agreement with the one obtained by Yang and Voke (2001) in their LES ($l_r = 5.2H$ at $Re = 1725$) with only a slight underestimation of -10%. For $\eta = 0.125$, a more significant underestimation of about -30% is found in this work by comparison with the typical value $l_r \approx 10H$ reported in the literature at higher Reynolds number for a sharp edge (see for instance Kiya and Sasaki, 1985; Suksangpanomrung et al., 2000; Abdalla and Yang, 2004). It is difficult to conclude about the reason of this discrepancy that could be simply due the difference of geometry, $\eta = 0.125$ being not small enough to corresponds to a sharp edge with $\eta = 0$. Another possibility is that present relatively low Reynolds number leads to more 2D primary instabilities with a resulting shortening of the bubble length. Moreover, the limited spanwise extension of the computational domain used here ($L_z = 6H$) could also contribute artificially to this behaviour.

Table 1
Recirculation length l_r, separation bubble height h_r, distance between the separation bubble centre and the separation point $\Delta x_c = x_c - x_0$, separation angle θ, maximum of the turbulent kinetic energy $k_{\max}$, distance between the upstream location of the contour $k = 1\% U_\infty^2$ and the separation point $\Delta x_{\min} = x_{\min} - x_0$, minimum value of the mean longitudinal velocity $U_{\min}$ (highest backflow). Present results are normalized by H and U_∞. Values obtained with ($u'_{\text{inflow}} = 0.1\% U_\infty$, left) and without ($u'_{\text{inflow}} = 0$, right) inflow perturbations.

	η	0.125	0.25	0.50	1
3D	l_r	6.8|7.3	5.8|7.4	4.8|6.7	4.7|7.6
	h_r	.90|.94	.77|.91	.57|.72	.43|.61
	$\frac{\Delta x_c}{l_r}$	.56|.55	.62|.67	.71|.75	.76|.81
	θ	40°|40°	32°|32°	23°|23°	15°|16°
	$k_{\max}$	.16|.17	.17|.16	.15|.15	.11|.11
	$\Delta x_{\min}$	1.3|1.2	1.8|2.8	2.1|3.6	2.9|4.9
	$U_{\min}$	-.38|-.30	-.34|-.34	-.29|-.30	-.23|-.25
2D	l_r	3.4|3.3	3.4|3.3	3.8|3.8	4.8|5.9
	h_r	.60|.60	.55|.55	.52|.51	.46|.55
	$\frac{\Delta x_c}{l_r}$	.52|.52	.54|.56	.66|.64	.69|.69
	θ	39°|39°	31°|31°	22°|22°	15°|15°
	$k_{\max}$	.30|.30	.27|.27	.21|.21	.15|.16
	$\Delta x_{\min}$	.07|.06	.17|.18	.58|.52	2.1|2.5
	$U_{\min}$	-.45|-.45	-.38|-.39	-.37|-.35	-.30|-.31

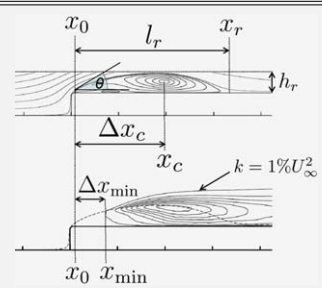

An interesting change in the structural features of the separation bubble is related to the relative location of its centre detected as the singular point (of zero velocity) corresponding to a focus that is neither divergent nor convergent for the present 2D geometry (Delery, 2001; Lamballais et al., 2008). The examination of Fig. 4 clearly shows that the centre moves toward the reattachment point as the curvature is decreased, for 3D as well as for 2D results. This information is confirmed quantitatively in Table 1 where the different values of the distance $\Delta x_c = x_c - x_0$ between the centre streamwise location x_c and the separation point are reported for each case with a renormalization by l_r. This trend can be interpreted as a consequence of the instability source that moves toward the reattachment zone at low curvature with the creation of an extended "dead flow" region in the upstream part of the separation bubble where the flow is virtually stationary. In contrary, when the curvature is increased, the upstream shifting of the bubble centre leads to a reduction of this quiet zone, suggesting a corresponding displacement of the instability source. Note also the more complex structure of the separation bubble at $\eta = 0.125$, 0.25 where a secondary recirculation region is unambiguously detected in 3D

at a location where non-negligible perturbations can already be suspected. This secondary bubble is always recovered in 2D, confirming that the bubble dynamics in 2D cases responds to different excitation mechanisms compared with 3D cases.

5. Turbulent kinetic energy

To have a better idea about the location of the main unsteady regions of the flow, turbulent kinetic energy contours are presented in Fig. 8 for 3D cases with inflow perturbations $u'_{\text{inflow}} = 0.1\%U_\infty$. Qualitatively, similar patterns are obtained from 3D DNS without inflow perturbations with a simple shifting of the contours further downstream, especially for the low curvature cases (see next section). The main values of the fluctuating kinetic energy k in 2D cases are reported in Table 1 for completeness without specific comments due to the very different nature of k production/dissipation for the 2D regime.

3D results exhibit (see Fig. 8) a rise of the turbulence levels as the curvature is increased, in agreement with the previous qualitative analysis based on instantaneous visualizations. The region for which k is significant is considerably enlarged for small η, with an increase of $k_{\max}$ up to +50% compared with the low curvature case $\eta = 1$. The location of $k_{\max}$ can be related to the separation bubble centre with a similar shifting toward the reattachment zone for low curvature cases. The move of the turbulent intensity suggests again a change of the instability source locations which drive the unsteady processes.

Additionally, it is worth noting that the upstream location $x_{\min}$ of the contour $k = 1\%U_\infty^2$ moves toward the separation point as the curvature is increased. This behaviour is shown by Table 1 where the distance $\Delta x_{\min} = x_{\min} - x_0$ is reduced by more than -50% for the highest curvature case compared with $\eta = 1$. Note that the forward peak of the contour $k = 1\%U_\infty^2$ suggests that primary instabilities are triggered in the separated shear layer, this view being qualitatively confirmed with the instantaneous visualizations. However, this peak is not exactly centred on the shear layer with a slight shift toward the wall. This feature, connected with the upstream/downstream influences on the bubble dynamics, is the main subject of the following three sections.

6. Influence of inflow perturbations

In this section, we consider the influence of the amplitude of the inlet excitation through comparisons between the cases with and without inflow perturbations. First, it is important to point out that the level of inlet excitation ($u'_{\text{inflow}} = 0.1\%U_\infty$) is relatively low in order to correspond to a weak residual turbulence in the main stream. This is in contrast with our previous study (Lamballais et al., 2008) on laminar separation where inflow fluctuations were 10 times higher in order to correspond to experiments in a water tunnel (Courtine et al., 2007). Here, the receptivity of the flow with respect to upstream fluctuations is discussed thanks to a comparison between results obtained with this slight upstream unsteady forcing and results free from any inflow perturbations except the numerical errors of significantly lower amplitude.

A strong sensitivity of the separation bubble with respect to inlet excitation can be noticed in Table 1 at low curvature. For instance, l_r is found to increase by more than +60% in 3D (+23% in 2D) for $\eta = 1$ when the inlet is free from perturbations, this strong effect being somewhat unexpected regarding the low level of inflow perturbations of the reference case. When the curvature of the front edge is more pronounced, this sensitivity of the bubble size is reduced with only a +7% increase of l_r at $\eta = 0.125$ when the inlet excitation is removed. For the 2D cases, l_r becomes nearly independent of the level of inflow fluctuations when $\eta \leqslant 0.5$. An illustration of these effects can be seen in Fig. 5. Concerning the bubble height, a similar behaviour is recovered with an increase of h_r when inflow perturbations are suppressed, this increase being clearly less marked for high curvature, with for instance +42% at $\eta = 1$ against only +4% at $\eta = 0.125$ in 3D DNS (see Table 1 and Fig. 7). These changes of the bubble size cannot be attributed to the separation angle θ that does not show any significant sensitivity with respect to the inlet excitation (see Table 1).

The sensitivity of the flow with respect to inflow perturbations can be interpreted as a feature of convective instability while the receptivity reduction can be associated with an absolutely unstable behaviour. From this view, 2D mechanisms are found to increase the efficiency of absolutely unstable processes that seem to dominate the overall dynamics of the separation bubble. However,

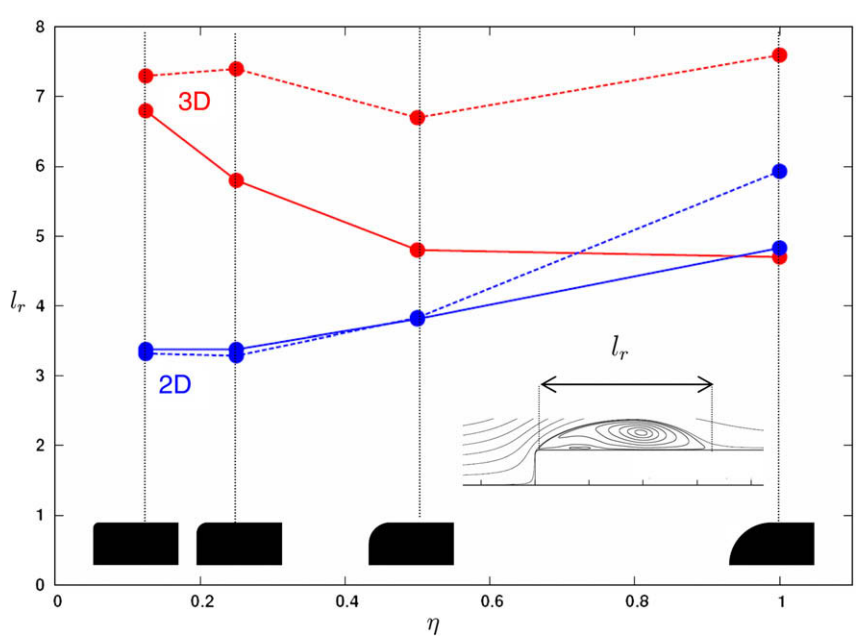

Fig. 5. Curvature and inlet excitation effects on the reattachment length l_r. Red lines: 3D DNS. Blue lines: 2D DNS. Solid lines: $u'_{\text{inflow}} = 0.1\%U_\infty$. Dashed lines: $u'_{\text{inflow}} = 0$ (without inflow perturbation). (For interpretation of the references to colour in this figure legend, the reader is referred to the web version of this article.)

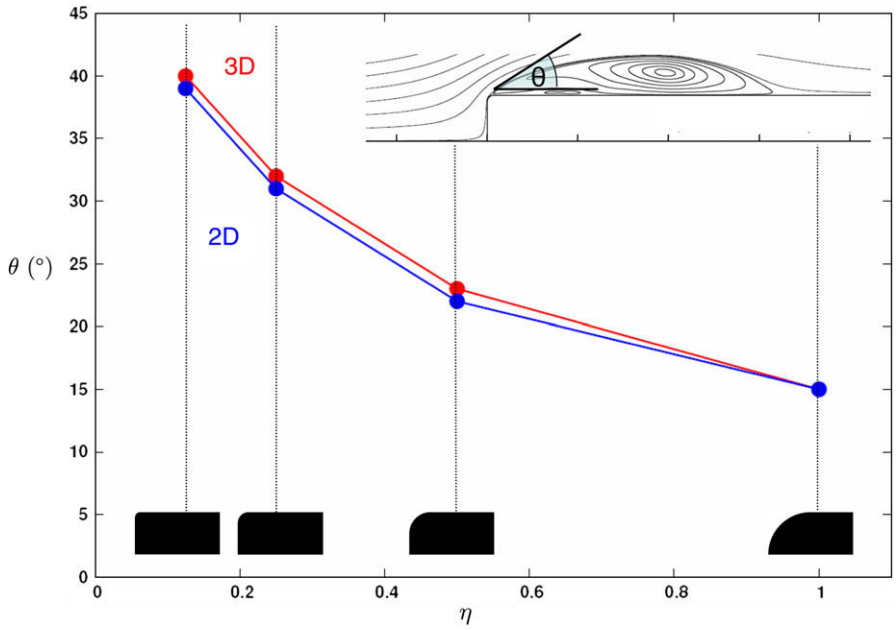

Fig. 6. Curvature effects on the separation angle θ. Red lines: 3D DNS. Blue lines: 2D DNS. $u'_{\text{inflow}} = 0.1\%U_\infty$. (For interpretation of the references to colour in this figure legend, the reader is referred to the web version of this article.)

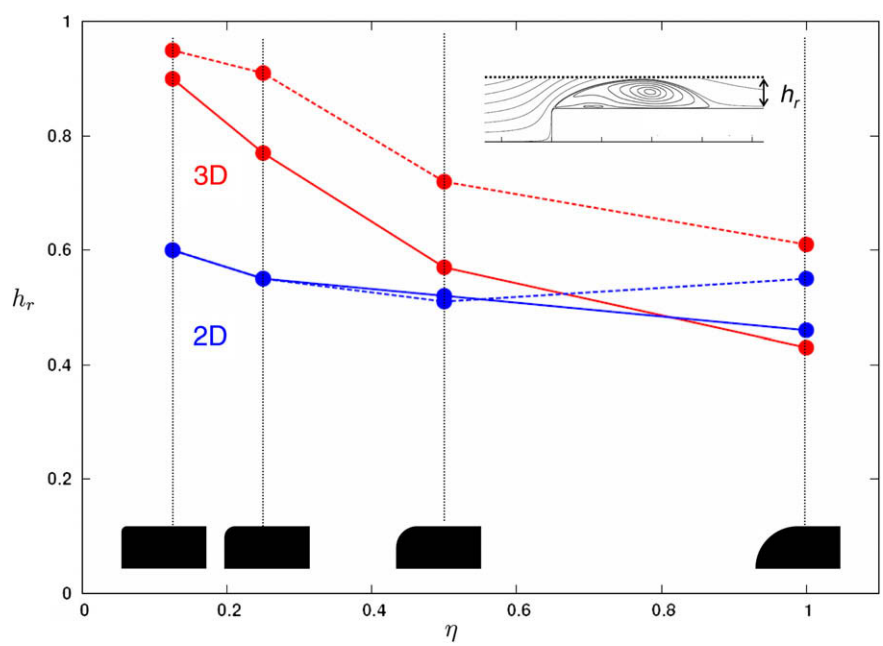

Fig. 7. Curvature and inlet excitation effects on the bubble height h_r. Red lines: 3D DNS. Blue lines: 2D DNS. Solid lines: $u'_{\text{inflow}} = 0.1\%U_\infty$. Dashed lines: $u'_{\text{inflow}} = 0$ (without inflow perturbation). (For interpretation of the references to colour in this figure legend, the reader is referred to the web version of this article.)

when 3D motions are allowed, the flow becomes unstable with respect to 3D perturbations, the resulting 3D dynamics being found more receptive to inflow fluctuations, especially for moderate curvature cases. To summarize, 2D mechanisms are found more efficient for the self-excitation of the flow but at the same time, they are dominated by 3D processes that reduce their efficiency while preserving the sensitivity of the flow with respect to inflow conditions, this sensitivity being gradually reduced when η is decreased.

An important observation is that with or without inflow perturbations, all the flow cases considered here reach a self-sustaining unsteady state. This ability of the flow to be self-excited suggests the occurrence of absolutely unstable mechanisms governing the separation bubble dynamics. This is in contrast with our previous study (Lamballais et al., 2008) where the removal of inlet excitation was found to lead to a transient stabilization of the flow with a considerable enlargement of the separation bubble, its proximity with the computational domain exit having prevented us to pursuit the simulation. Here, this phenomenon is not recovered. This change of behaviour can be attributed to the use of a higher Reynolds number ($Re = 2000$ in this study against $Re = 1250$ in Lamballais et al., 2008) that seems to change the stability properties of the flow in favour to absolute instability mechanisms. This observation conciliates partly our previous and present results with the ones of (Yang and Voke, 2001) who considered an intermediate Reynolds number ($Re = 1725$) with $\eta = 1$. They reported

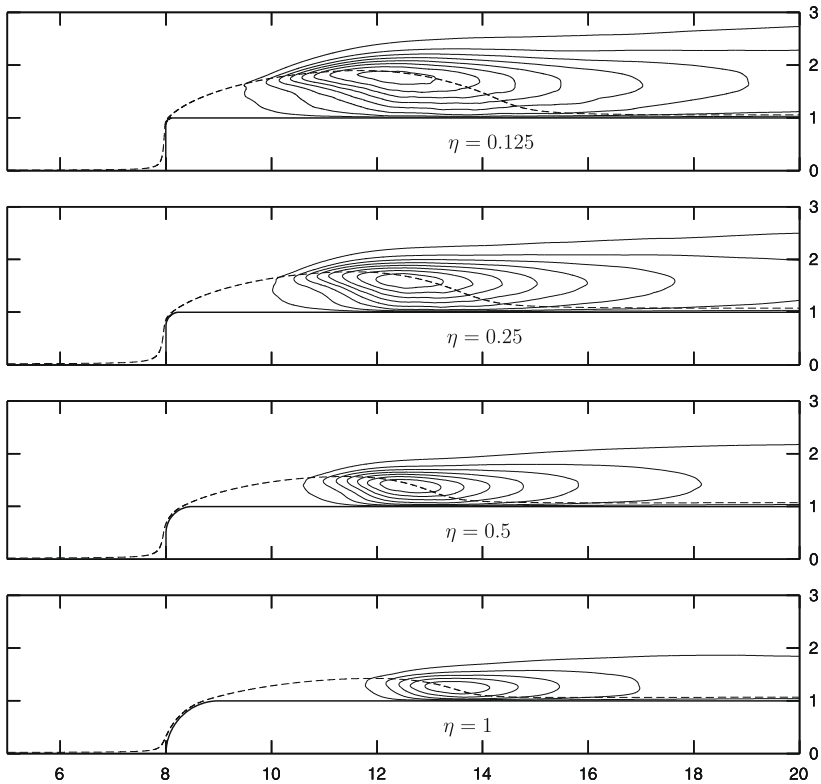

Fig. 8. Turbulent kinetic energy k contours for $\eta = 0.125,\ 0.25,\ 0.5,\ 1$ (contour levels from $0.01U_\infty^2$ by step of $0.02U_\infty^2$). Results from 3D DNS with inflow perturbations $u'_{\text{inflow}} = 0.1\%U_\infty$. The dashed line shows the delimiting streamline of the bubble.

that their flow was able to reach a self-sustaining state (in line with our conclusions) but they observed no significant influence of the inflow perturbations, whereas this influence is found substantial in our simulations.

To confirm present effects of inflow perturbations, two additional simulations have been conducted for $\eta = 0.25$ and $\eta = 1$ with a stronger inlet excitation of $u'_{\text{inflow}} = 1\%U_\infty$. For $\eta = 1$, l_r is found to decrease by -32% (compared to the case $u'_{\text{inflow}} = 0.1\%U_\infty$) with $l_r = 3.2H$. For $\eta = 0.25$, a reduction of l_r is also recovered with $l_r = 4.2H$, the corresponding relative decrease being of -28%. The corresponding effects on the bubble shape are shown in Fig. 9 where the cases without inlet excitation are also plotted. These additional tests show that the reduction of the inflow sensitivity with the curvature increase remains preserved even for high amplitude inflow perturbations.

7. Deterministic response with respect to cyclic inlet excitation

In this section, we follow again the procedure proposed in (Lamballais et al., 2008) to estimate the receptivity of the bubble dynamics through a deterministic analysis of its response with respect to a cyclic inlet excitation. As already mentioned in Section 2, the inflow noise used at the inlet has been generated to verify a periodicity over a cycle $T = 40H/U_\infty$. Recycling twice this noise leads to two sets of flow realization more or less correlated depending on the determinism level with respect to inflow conditions. The principle of the deterministic analysis is to compare two flow realizations at the same time inside a cycle but for two different cycles. In the region where the flow is purely deterministic with respect to inflow conditions, results are expected to be identical, while in other regions, a gradual decorrelation can occur.

This information can be computed statistically using a two-time correlation where the time separation corresponds to the T-periodicity of inflow conditions. Using an average in the homogeneous z-direction and in time over a cycle T (denoted by the operator $\langle\cdot\rangle_{t,z}$), a correlation coefficient $C(x,y)$ based on the fluctuating velocity $\mathbf{u}'(\mathbf{x},t)$ can be defined, with

$$C(x,y) = \frac{\langle \mathbf{u}'(\mathbf{x},t)\cdot\mathbf{u}'(\mathbf{x},t+T)\rangle_{t,z}}{\sqrt{\left\langle \mathbf{u}'(\mathbf{x},t)^2\right\rangle_{t,z}}\sqrt{\left\langle \mathbf{u}'(\mathbf{x},t+T)^2\right\rangle_{t,z}}} \tag{1}$$

where $\cdot$ is a scalar product involving the three velocity components. In regions where this coefficient is one, the flow is T-periodic and can be said fully deterministic with respect to inflow conditions. Smaller values of $C(x,y)$ indicate a decorellation and a corresponding decrease of this type of determinism.

In practice, $C(x,y)$ has been computed here using two sets of 16 velocity fields from two consecutive cycles which have been pairwise correlated. The use of only two cycles prevents us to reach a fully converged estimation of $C(x,y)$, especially near a singular point (of zero mean velocity) where a very slow nonstationarity can lead to an artificial correlation (or even an anticorrelation with negative C) between two cycles. In practice, we only have observed this artefact in the neighbourhood of the separation point inside the bubble, a region where the flow is almost purely stationary with very weak velocity fluctuations. In the present analysis, this local lack of convergence is considered rather unimportant.

Two examples of $C(x,y)$ are presented in Fig. 10 for the case $\eta = 1$ with two levels of inflow perturbations $u'_{\text{inflow}} = 0.1\%,\ 1\%U_\infty$. For the highest inlet excitation, in agreement with our previous study based on the same flow with a lower Reynolds number (Lamballais et al., 2008), the region outside the bubble and its wake is found to be fully deterministic with $C \approx 1$ (see Fig. 10). However, inside the bubble, correlation levels are found strongly reduced here compared with the case presented in Lamballais et al. (2008). This important change, observed for the same geometry ($\eta = 1$), can be attributed to the increase of the Reynolds

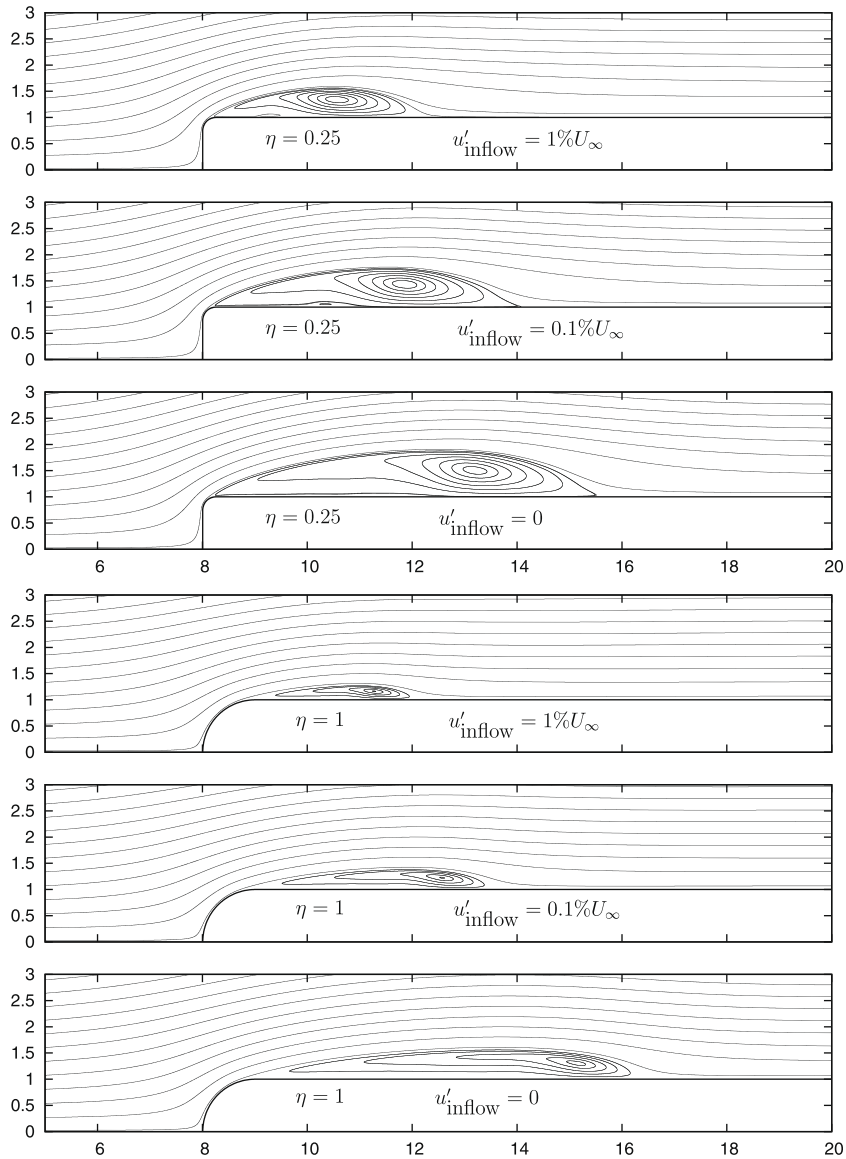

Fig. 9. Comparison among the mean streamlines obtained with three different levels of inflow perturbation $u'_{\text{inflow}} = 0,\ 0.1,\ 1\%U_\infty$ for $\eta = 0.25, 1$ (3D DNS results).

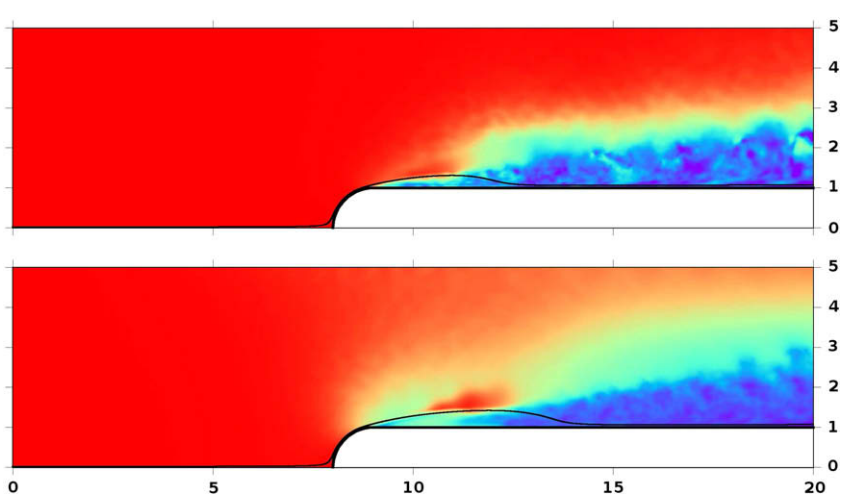

Fig. 10. Maps of the correlation coefficient $C(x, y)$ for $\eta = 1$ with $u'_{\text{inflow}} = 1\%U_\infty$ (top) or with $u'_{\text{inflow}} = 0.1\%U_\infty$ (bottom). High values ($C \approx 1$) are in red while low values ($C \approx 0$) are in blue. The black line shows the delimiting streamline of the bubble.

number, while being consistent with the appearance of a self-sustained regime of the bubble dynamics found in this study at $Re = 2000$ but not previously observed at $Re = 1250$ in Lamballais et al. (2008). From this point of view, the present deterministic analysis based on the correlation coefficient C seems to be an interesting tool to identify the presence of self-excitation mechanisms through the detection of their direct consequences on the chaotic behaviour of the bubble.

For $u'_{\text{inflow}} = 0.1\% U_\infty$, unexpected uncorrelated regions are detected above the bubble and further downstream far from the body. The origin of this correlation loss is difficult to determine, especially its physical relevancy. In practice, it can be observed that these low values of C observed outside from the active region of the flow corresponds to very low levels of turbulent kinetic energy. Hence, very low amplitude velocity fluctuations are found here to be weakly deterministic. Physically, this behaviour can be accepted, but numerical errors could also be responsible of this correlation loss when velocity fluctuations are too weak compared with the machine accuracy or with the truncation error. Note in particular that the present definition (1) of $C(x, y)$ cannot behave correctly when $\mathbf{u}' \to 0$ due to its denominator. To eliminate this ambiguity from the following analysis, C is now only plotted in regions where a significant turbulent kinetic is produced by choosing the threshold $k > 10^{-4} U_\infty^2$.

The corresponding maps are presented in Fig. 11 for $\eta = 0.25,\ 0.5,\ 1$ with $u'_{\text{inflow}} = 0.1\% U_\infty$ (low amplitude inlet excitation). A comparison among these three cases reveals that the curvature strongly changes the determinism of the flow in the bubble region. First, if only the maximum value of C is considered (by excluding inactive regions where $k < 10^{-4} U_\infty^2$ as already mentioned), we obtain $C_{\max} \approx 95\%,\ 70\%,\ 45\%$ for $\eta = 1,\ 0.5,\ 0.25$ respectively. This strong decrease of $C_{\max}$ confirms quantitatively that self-excitation mechanisms are more efficient when the curvature is high, leading to a progressive loss of determinism with respect to inflow conditions. Note that maximum values of C are found in the upper part of the bubble for the three cases, in the region of Kelvin–Helmoltz vortex formation (see Fig. 10). In the bubble core, a strong decorrelation with an extended zone where $C < 10\%$ can be observed for $\eta = 0.25,\ 0.5$, whereas in the same region, $C > 50\%$ can be observed for $\eta = 1$. More quantitatively, the mean value of C inside the bubble region (defined using the delimiting streamline) is found to be $C_m \approx 50\%,\ 10\%,\ 10\%$ for $\eta = 1,\ 0.5,\ 0.25$ respectively. The present deterministic analysis confirms again the reduction of the inflow receptivity of the bubble when the curvature is increased, a feature that can be related to the reinforcement of self-excitation mechanisms, these latter being expected more chaotic.

8. Reverse flow inside the bubble

The intensity of the reverse flow inside the bubble can provide a preliminary idea about the more or less convectively unstable nature of present bubble separations. In Table 1 are reported the highest backflow velocities $U_{\min}$ for each case. The velocity profiles at the corresponding x-locations are presented in Fig. 12 for the 2D and 3D results obtained with inflow perturbations. Note that very similar profiles are obtained for the cases without inflow perturbations, as suggested by the very close values of $U_{\min}$ reported in Table 1 with and without inlet excitation.

The major effect on $U_{\min}$ is due to the curvature that is found to increase gradually the backflow (up to +65%) from $\eta = 1$ to $\eta = 0.125$ both in 2D and 3D. This behaviour is consistent with the previous comments suggesting the reinforcement of absolutely unstable mechanisms when the curvature is increased. This trend

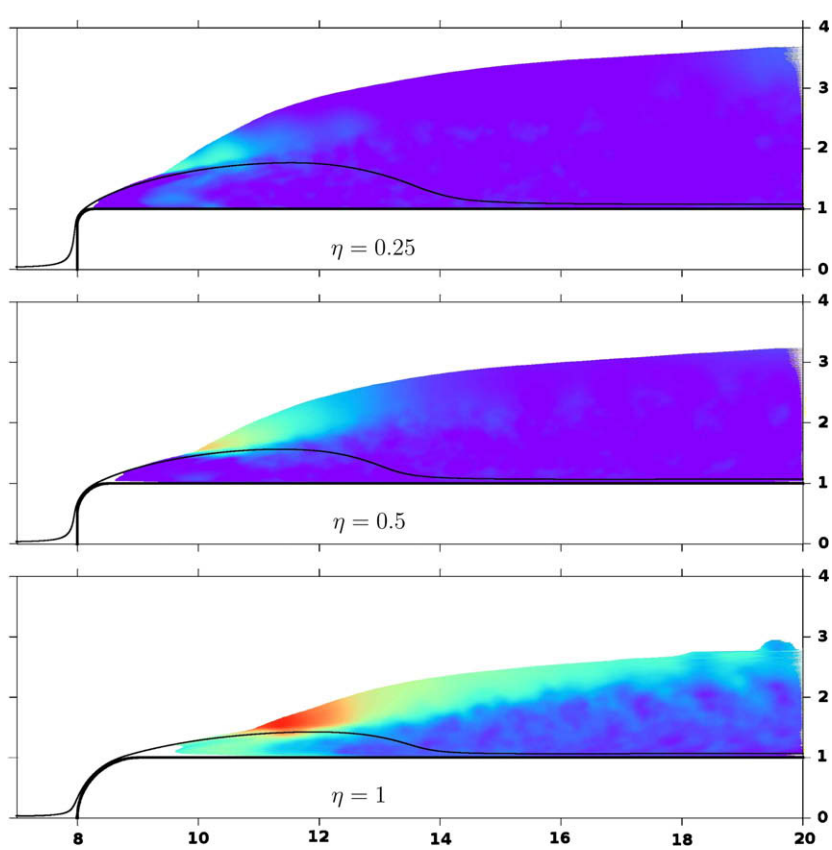

Fig. 11. Maps of the correlation coefficient $C(x, y)$ for $\eta = 0.25,\ 0.5,\ 1$ with $u'_{\text{inflow}} = 0.1\% U_\infty$. High values ($C \approx 1$) are in red while low values ($C \approx 0$) are in blue. The black line shows the delimiting streamline of the bubble. $C(x, y)$ is only shown for regions where $k > 10^{-4} U_\infty^2$.

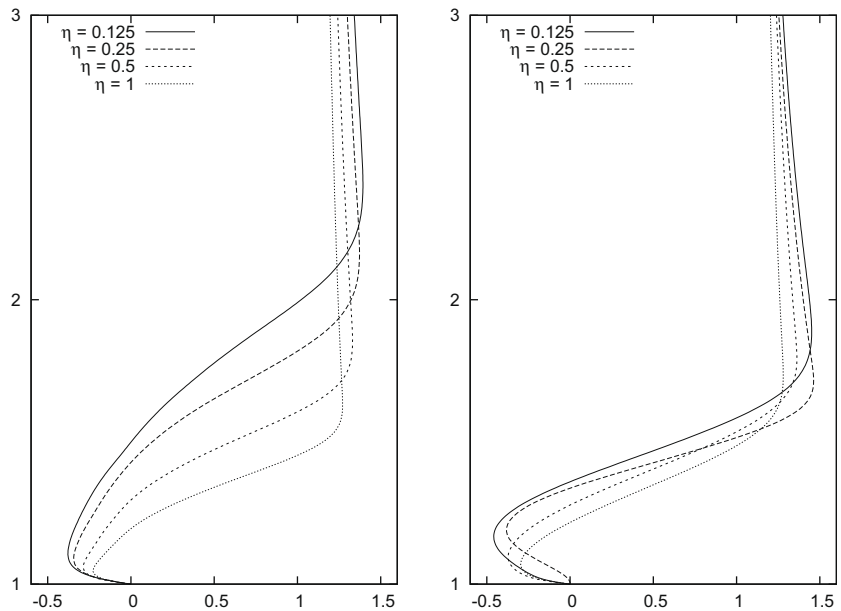

Fig. 12. Comparison of mean longitudinal velocity profiles for $\eta = 0.125,\ 0.25,\ 0.5,\ 1$ at the streamwise location where the reverse flow is the strongest. Results from 3D (left) and 2D (right) DNS with inflow perturbations $u'_{\text{inflow}} = 0.1\% U_\infty$.

occurs in 3D as well as in 2D, but the reverse flow is found to be stronger for 2D cases and more concentrated in the near-wall region, consistently with the reduction of the bubble height h_r when 3D motions are prevented (see Table 1 and Fig. 7).

A final remark about the backflow can be made about the high values of $U_{\min}$ (in absolute value) even for the low curvature case in 3D. The minimal reverse flow is found to be 23% of U_∞, a higher value than the critical value of 15% obtained by Alam and Sandham (2000) for the margin of convective/absolute stability in their bubble. Note that even a normalization using the maximum velocity at the same streamwise location as $U_{\min}$ leads to backflow always stronger than 18% for all the cases considered here. Despite the significant differences of present separation bubbles by comparison with Alam and Sandham (2000), present strong reverse flow suggests again the existence of an absolute instability region that governs the dynamics of all the separation bubbles presented in this work.

9. Conclusion

The generic half-body considered here can be viewed as a thick half-plate with a front edge more or less rounded. In this study, we examine only the effect of the front-edge curvature by keeping constant the Reynolds number based on the half-body height H. To have a wide view of these effects, almost one order of magnitude separates the highest curvature from the lowest one considered in this paper.

For all the cases treated, a separating–reattaching flow is obtained with a common feature of self-excitation in the separation bubble revealed by the ability of each flow to lead to self-sustaining unsteady processes without the need of any inlet excitation. Despite this common property, the basic change of the front-edge curvature is found to deeply influence the bubble dynamics.

These modifications can be observed directly on the mean flow through the enlargement of the bubble size controlled by antagonist effects associated with the increase of the separation angle combined with the turbulence reinforcement as the curvature is increased. An additional effect is the strong increase of turbulent kinetic energy levels in the bubble region for high curvature.

The comparison between 2D and 3D DNS results shows that 3D motions dominate the bubble dynamics while decreasing the efficiency of self-excitation mechanisms, the artificial purely 2D dynamics being found to promote absolutely unstable processes. For the more realistic 3D DNS, a more marked absolutely unstable character is observed at high curvature, with a clear reduction of the sensitivity of the flow with respect to inflow conditions. In terms of curvature effects, 2D DNS is found to lead to irrelevant predictions, especially the reverse influence on the reattachment length compared with 3D DNS results.

Comparisons between cases with and without inflow perturbations show that the receptivity of the flow with respect to upstream conditions is decreased for high curvature. This behaviour can be observed directly on the mean flow or on turbulent statistics. A deterministic analysis of the bubble dynamics response with respect to cyclic inlet excitation confirms this loss of inflow receptivity as the curvature is increased. The associated strong increase of the backflow near the bottom of the bubble suggests the reinforcement of the absolutely unstable character of the separated flow, this view being consistent with the loss of inflow receptivity as the curvature is increased.

To get quantitative information about the curvature influence in the absence of any turbulence fluctuation, it could be interesting to compute the steady flow for each body at the same Reynolds number. Technically, this unstable solution should be reachable using the present numerical code with the help of the method proposed by Åkervik et al. (2006). Such an artificial time truncation could be complementary to the present 3D truncation offered by 2D DNS. In addition to the comparison among the steady flows obtained for each leading-edge curvature (considered through the bubble features $l_r,\ h_r,\ \theta,\ U_{\min}$, etc.), the access to the base flows would allow a stability analysis (preferably with a global viewpoint) that could be helpful to better understand the various mechanisms, possibly antagonist, responsible of the bubble transformations.

Acknowledgements

This work was granted access to the HPC resources of IDRIS/CINES/CCRT under the allocation 2009-020912 made by GENCI

(Grand Equipement National de Calcul Intensif). The authors are grateful to A. Spohn for his precious advices on this work.

References

Åkervik, E., Brandt, L., Henningson, D.S., Hœpffner, J., Marxen, O., Schlatter, P., 2006. Steady solutions of the Navier–Stokes equations by selective frequency damping. Phys. Fluids 18 (6), 068102.

Abdalla, I.E., Yang, Z., 2004. Numerical study of the instability mechanism in transitional separating–reattaching flow. Int. J. Heat Fluid Flow 25, 593–605.

Adams, N.A., Shariff, K., 1996. A high-resolution hybrid compact-ENO scheme for shock–turbulence interactions problems. J. Comput. Phys. 127, 27–51.

Alam, M., Sandham, N.D., 2000. Direct numerical simulation of short laminar bubbles with turbulent reattachment. J. Fluid Mech. 403, 223–250.

Courtine, S., Spohn, A., Bonnet, J.-P., 2007. Vortex dynamics in the reattaching flow of separation bubbles with variable aspect ratio. Advances in Turbulence XI, vol. 117. Springer, Berlin, Heidelberg, pp. 370–372.

Delery, J.-M., 2001. Robert Legendre and Henri Werlé: toward the elucidation of three-dimensional separation. Annu. Rev. Fluid Mech. 33, 129–154.

Kiya, M., Sasaki, K., 1985. Structure of large-scale vortices and unsteady reverse flow in the reattaching zone of a turbulent separation bubble. J. Fluid Mech. 154, 463–491.

Laizet, S., Lamballais, E., 2009. High-order compact schemes for incompressible flows: a simple and efficient method with quasi-spectral accuracy. J. Comput. Phys. 228, 5989–6015.

Laizet, S., Lamballais, E., Vassilicos, J.C., 2010. A numerical strategy to combine high-order schemes, complex geometry and parallel computing for high resolution DNS of fractal generated turbulence. Comput. Fluids 39 (3), 471–484.

Lamballais, E., Silvestrini, J., Laizet, S., 2008. Direct numerical simulation of a separation bubble on a rounded finite-width leading edge. Int. J. Heat Fluid Flow 29 (3), 612–625.

Parnaudeau, P., Carlier, J., Heitz, D., Lamballais, E., 2008. Experimental and numerical studies of the flow over a circular cylinder at Reynolds number 3900. Phys. Fluids 20 (085101).

Suksangpanomrung, A., Djilali, N., Moinat, P., 2000. Large-eddy simulation of separated flow over a bluff rectangular plate. Int. J. Heat Fluid Flow 21, 655–663.

Yang, Z., Voke, P., 2001. Large-eddy simulation of boundary-layer separation and transition at a change of surface curvature. J. Fluid Mech. 439, 305–333.